34. Allegra, J. C., Stein, A. & Allen, G. F. Tracer diffusion and shear viscosity for the system isobutyric acid-water near the critical mixing point. *J. Chem. Phys.* **55,** 1716–1720 (1971).
35. Smith, R. S., Huang, C. & Kay, B. D. Evidence for molecular translational diffusion, during the crystallization of amorphous solid water. *J. Phys. Chem. B* **101,** 6123–6126 (1997).
36. Smith, R. S. & Kay, B. D. Evidence for the existence of supercooled liquid water at 150 K. *Nature* **398** (in the press)
37. Roberts, C. J., Karayiannekis, C. & Debenedetti, P. G. Liquid-liquid immiscibility in single-component network-forming fluids: Model calculations and implications for polyamorphism in water. *Ind. Eng. Chem. Res.* **37,** 3012–3022 (1998).

Acknowledgements. This work was supported by the NSF DMR Solid State Chemistry program.

Correspondence and requests for materials should be addressed to C.A.A. (e-mail: caa@asu.edu).

Control of crystal nucleation by patterned self-assembled monolayers

Joanna Aizenberg*, Andrew J. Black† & George M. Whitesides†

** Bell Laboratories, Lucent Technologies, Murray Hill, New Jersey 07974, USA*
† Department of Chemistry and Chemical Biology, Harvard University, Cambridge, Massachusetts 02138, USA

An important requirement in the fabrication of advanced inorganic materials, such as ceramics and semiconductors, is control over crystallization[1–4]. In principle, the synthetic growth of crystals can be guided by molecular recognition at interfaces[5–16]. But it remains a practical challenge to control simultaneously the density and pattern of nucleation events, and the sizes and orientations of the growing crystals. Here we report a route to crystal formation, using micropatterned self-assembled monolayers[17,18], which affords control over all these parameters. We begin with a metal substrate patterned with a self-assembled monolayer having areas of different nucleating activity—in this case, an array of acid-terminated regions separated by methyl-terminated regions. By immersing the patterned substrates in a calcium chloride solution and exposing them to carbon dioxide, we achieve ordered crystallization of calcite in the polar regions, where the rate of nucleation is fastest; crystallization can be completely suppressed elsewhere by a suitable choice of array spacing, which ensures that the solution is undersaturated in the methyl-terminated regions. The nucleation density (the number of crystals formed per active site) may be controlled by varying the area and distribution of the polar regions, and we can manipulate the crystallographic orientation by using different functional groups and substrates.

We patterned self-assembled monolayers (SAMs) on the metal substrates by microcontact printing with an elastomeric stamp[18,19] that had a relief structure consisting of a square array of raised circles with diameter d and periodicity p (Fig. 1a): as "inks", we used 10 mM solutions of $HS(CH_2)_nX$ ($X = CO_2H$, SO_3H, OH) in ethanol. The surface was then washed with a 10 mM solution of $HS(CH_2)_{15}CH_3$ in ethanol to passivate the areas that had not contacted the stamp. We focus on the crystallization of calcite ($CaCO_3$). The general principles of calcite formation have been extensively studied, due to the importance of this mineral in nature as a structural material[20,21]. The patterned substrates were supported upside-down in a calcium chloride solution to ensure that only particles grown on the SAM would be bound to the surface, and placed in a closed desiccator with vials of solid ammonium carbonate in the bottom[6] (Fig. 1b).

The surfaces decorated with crystals were examined using a scanning electron microscope (SEM) operating at 15 keV. The crystallographic orientations of the crystals relative to the surface were determined using X-ray diffraction and morphological analysis[20]. Figure 1c shows a low-magnification micrograph of the pattern of calcite crystals formed on a sample SAM—printed 35-μm circles of $HS(CH_2)_{15}CO_2H$ in a background of $HS(CH_2)_{15}CH_3$—supported on Ag ($[Ca^{2+}] = 25$ mM, crystallization time $t = 30$ min). Crystallization is restricted to well defined, CO_2^--terminated regions, and does not occur on the CH_3-terminated area of patterned surfaces, although the solution was supersaturated in $CaCO_3$ and crystal formation occurred on both CO_2^-- and CH_3-terminated SAMs when they were not patterned (Fig. 1c, insets).

By adjusting the pattern, density and sizes of features in the stamp, the concentration of the crystallizing solution, and the

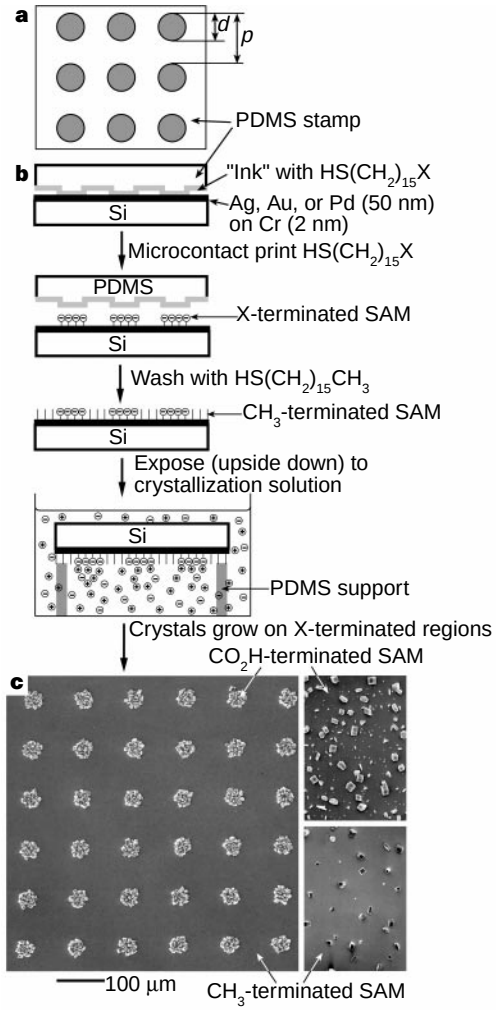

Figure 1 Experimental design of crystallization on patterned SAMs. **a**, Relief structure of the patterned PDMS stamps used for microcontact printing. **b**, Schematic presentation of the experimental steps. Dimensions are not to scale. **c**, Scanning electron micrograph (SEM) of the sample patterned surface–printed circles of $HS(CH_2)_{15}CO_2H$ in a background of $HS(CH_2)_{15}CH_3$ supported on Ag(111)–overgrown with calcite crystals. For these experimental conditions–$[Ca^{2+}] = 25$ mM, pH ~7, crystallization time $t = 30$ min–the nucleation is highly specific to the acid-terminated regions, and the crystals are remarkably uniform in size and nucleation density. The insets illustrate the wide distribution of sizes of crystals formed on the non-patterned SAMs presenting the same terminal groups to a solution with the same value of $[Ca^{2+}]$. To prepare substrates, silicon wafers (test grade, n or p type, Silicon Sense, Nashua, NH) were coated with 2.5 nm of Cr, to promote adhesion, and then with metal (Ag, Au, Pd; typically ~50 nm) using an electron beam evaporator (base pressure 10^{-7} torr). The stamps were prepared by casting and curing poly(dimethylsiloxane) (PDMS) against rigid masters bearing a photoresist pattern formed using conventional lithographic techniques[18,19]. Calcite crystals formed on diffusion of carbon dioxide and ammonia vapours into the $CaCl_2$ solution.

© 1999 Macmillan Magazines Ltd

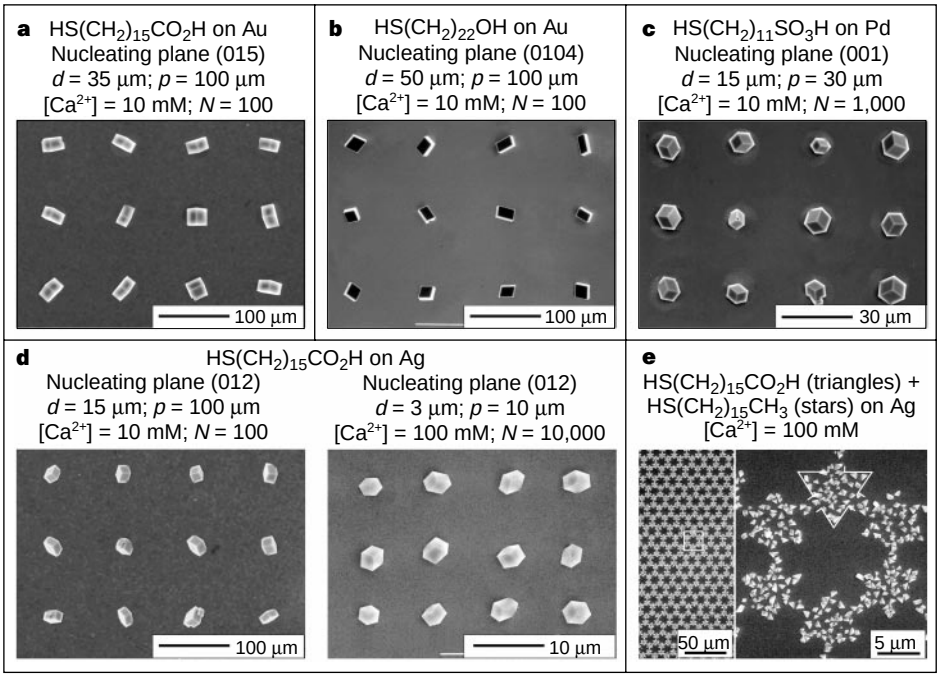

Figure 2 Ordered two-dimensional arrays of single calcite crystals. The densities of nucleation, uniform sizes and crystallographic orientation are controlled by the micropatterned SAMs consisting of regions of $HS(CH_2)_nX$ and $HS(CH_2)_{15}CH_3$. The density and sizes of features in the stamp and the concentration of the crystallizing solution were chosen to ensure the formation of one crystal per printed site. **a**, Arrays of crystals with the density of nucleation $N \approx 100$ crystals mm^{-2} grew selectively from the (015) plane on SAMs of $HS(CH_2)_{15}CO_2H$ supported on Au(111). **b**, Arrays of crystals with the density of nucleation $N \approx 100$ crystals mm^{-2} grew selectively from the (104) plane on SAMs of $HS(CH_2)_{22}OH$ supported on Au(111). **c**, Arrays of crystals with the density of nucleation $N \approx 1{,}000$ crystals mm^{-2} grew selectively from the (001) plane on SAMs of $HS(CH_2)_{11}SO_3H$ supported on Pd. **d**, Arrays of crystals nucleated selectively from the (012) plane on SAMs of $HS(CH_2)_{15}CO_2H$ supported on Ag(111) with various densities of nucleation: $N \approx 100$ crystals mm^{-2} (left) and $N \approx 10{,}000$ crystals mm^{-2} (right). **e**, An example of the fabrication of another complex crystalline pattern: a continuous, polycrystalline structure formed on SAMs consisting of a hexagonal array of 'stars' of $HS(CH_2)_{15}CH_3$ ($d = 12\,\mu m$, $p = 15\,\mu m$) in a field of $HS(CH_2)_{15}CO_2H$ on Ag(111). The low-magnification SEM (left) illustrates the high fidelity of the procedure, and the high-magnification fragment (right) shows the formation of uniform crystals of sub-micrometre sizes.

functionality of the surface of the SAM, we could control the most important characteristics of the crystallization process: that is, the location and density (N) of nucleating regions on the surface, the number (n) of crystals that nucleated within each region, and the crystallographic orientation of these crystals. Figure 2a–d shows several examples of ordered arrays of single calcite crystals ($n = 1$) with controllable densities of nucleation ($N \approx 100$, 1,000 and 10,000 crystals mm^{-2}) and crystallographic orientation (crystals nucleated specifically from the (015), (104), (001) and (012) planes on SAMs of Au/$HS(CH_2)_{15}CO_2H$, Au/$HS(CH_2)_{22}OH$, Pd/$HS(CH_2)_{11}SO_3H$ and Ag/$HS(CH_2)_{15}CO_2H$, respectively).

Control of orientation is based on our observation that SAMs terminated in different functional groups, as well as SAMs of a single thiol supported on different metal substrates, induce calcite nucleation from specific crystallographic planes and cause growth to occur in different crystallographic directions. The orientation of crystals is highly uniform for each SAM (the percentage of oriented crystals, estimated by morphological analysis of five random areas bearing ~40 crystals each, was 97–98% with standard deviation of 2–3%), an observation implying that the atomic-level interfacial structure is controlling the nucleating plane of the crystals. The selectivity of the oriented growth of calcite induced by the X-terminated SAMs is higher than that induced by Langmuir monolayers or polymer surfaces terminated in the same functional groups[6,7,11,12,16], due, we presume, to the more ordered structure of SAMs. SAMs terminated in different functional groups and/or supported on different substrates have different structural parameters[17]. The correlation between the structures of SAMs and crystal planes they nucleate suggests that face-selective nucleation stems from a match between the pattern and orientation of ions adsorbed on the organic surface and those in the nucleating crystal plane[6,9,10]. The method described here makes it possible, to our knowledge for the first time, to combine area-selective nucleation with highly specific growth of crystals in a single crystallographic direction.

The ability to form one crystal per active site ($n = 1$) is based on our observation that at constant concentration, the number of crystals, n, within each active nucleation region depended linearly upon its area (Fig. 3). This relationship makes it possible to determine the value of n by choosing the size, d, of the raised features in the stamp (Fig. 1a), and therefore provides precise control over the nucleation density.

A comparison between the arrays of crystals grown on patterned surfaces (Fig. 2a–d) and arrays grown on homogeneous, non-patterned SAMs (Fig. 1c, insets) highlights another advantage of this method—formation of crystals with similar sizes that reflect nucleation in different locations at similar times. We infer, therefore, that patterning surfaces with SAMs in regular arrays makes it possible to achieve control over many of the crucial aspects of nucleation and crystal growth. To our knowledge, Fig. 2 shows the first examples of periodic arrays of discrete crystals with controlled densities and location of nucleation, and with uniform sizes and crystallographic orientations. These arrays formed reproducibly in more than 10–20 repetitions.

This method is not limited to the nucleation of crystals on isolated regions. We are able to grow calcite crystals on SAMs having a range of patterns with sizes of features from submillimetre to submicrometre. Figure 2e shows an example of a complex pattern of calcite crystals grown on a surface having a pattern of interconnected triangles of carboxylic-acid-terminated SAM in a field of methyl-terminated SAM; the crystals follow the geometry of the underlying active nucleating regions with good fidelity. An earlier attempt to perform patterned crystallization on electron-beam-

© 1999 Macmillan Magazines Ltd

damaged SAMs[13] resulted in edge resolution of 2 μm. Our method generates patterns of crystals with edge resolution of a few hundred nanometres.

We suggest that high-resolution crystallization on the X-terminated regions—and the absence of nucleation on the CH_3-terminated regions—of patterned SAMs reflects the influence of mass transport. The rate of nucleation on SAMs terminated in polar groups is faster than on methyl-terminated SAMs. As soon as crystal growth begins in a polar region, mass transport to the growing crystals depletes calcium and carbonate ions over the local methyl-terminated region to the point of undersaturation. In surface growth models, the regime in which growth occurs on the surface with predeposited islands is usually referred to as submonolayer, or island, epitaxy[22]. The model that describes the growth behaviour in such systems—the DDA (deposition, diffusion and aggregation) model—predicts a characteristic length scale for a diffusion-limited, island-specific epitaxy: $l_d \approx (D/F)^{1/4}$, where l_d (cm) defines the size of the region where deposition does not occur, D ($cm^2\,s^{-1}$) is a diffusion coefficient and F ($cm^{-2}\,s^{-1}$) is a flux of particles (ions, atoms or molecules). In our system, l_d corresponds to the distance from the active nucleating region at which the local concentration of the solution (depleted by the mass transport to the growing crystals) approaches the saturation level for the nucleation of calcite on the slowly nucleating region of the SAM (Fig. 4a). The inhibition of nucleation would, therefore, appear only within a distance, l_d, from the edge of the active region. To test this conclusion, we performed crystallization on a methyl-terminated surface with one isolated region terminated in carboxylic acids. The experimental conditions—$[Ca^{2+}] = 25$ mM, $d = 35$ μm, crystallization time $t = 30$ min—were chosen to correspond to Fig. 1c. Solving the diffusion equation, $\partial c/\partial t = D\partial^2 c/\partial x^2$ (where c is the concentration and x is the position), for these specific parameters and assuming that the concentration of the saturated solution (c_{sat}) ≈ 2–2.5 mM, we estimated the size of the depletion region as $l_d = 80$–100 μm. Indeed, in Fig. 4b crystallization of calcite is observed in the predicted pattern, with no detectable nucleation within ~80 μm of the active region. Outside this area, nucleation occurs in a manner similar to that on non-patterned methyl-terminated surfaces (Fig. 1c, inset). For distances between the features, $p < 2l_d$, the solution over the slowly nucleating regions is effectively undersaturated (Fig. 4c), and there is no nucleation in these areas (as shown in Fig. 1c, where $p = 100\,\mu m < 2l_d = 160\,\mu m$).

Diffusion-controlled growth of calcite in nature is believed to be controlled locally by specialized macromolecules[21]. The power of our approach to crystallization is, therefore, its ability simultaneously

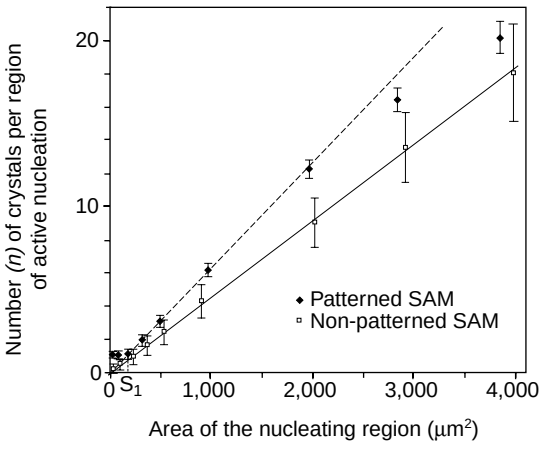

Figure 3 Average number of crystals nucleated per active region as a function of area, for patterned and non-patterned SAMs. The difference in standard deviation reflects the higher uniformity of the nucleation density on patterned SAMs than on non-patterned SAMs. For a large range of sizes of active regions of patterned SAMs (d = 15–50 μm), the average number of crystals nucleated per active region, n, is proportional to the area of the nucleating region (dashed line). As d increases, the nucleation densities decrease and approach the corresponding values for non-patterned SAMs (solid line). For small nucleating regions ($S \leq S_1$), the number of crystals nucleated per active region is constant ($n = 1$) irrespective of the area; this observation suggests that the size of the printed features is much larger than the critical size of the nucleation site for calcite. Calcite crystals were grown on nine patterned surfaces consisting of printed circles of $HS(CH_2)_{15}CO_2H$ in a background of $HS(CH_2)_{15}CH_3$ supported on Ag(111) (diameters of circles, d, were 5, 10, 15, 20, 25, 35, 50, 60 and 70 μm). For each surface, one 7 × 7-array of CO_2H-terminated circles was used for statistics (49 points) to determine the average number of crystals per nucleating spot and the standard deviation. We compared these data to the statistical results of the growth of calcite on non-patterned SAMs of $HS(CH_2)_{15}CO_2H$ supported on Ag(111).

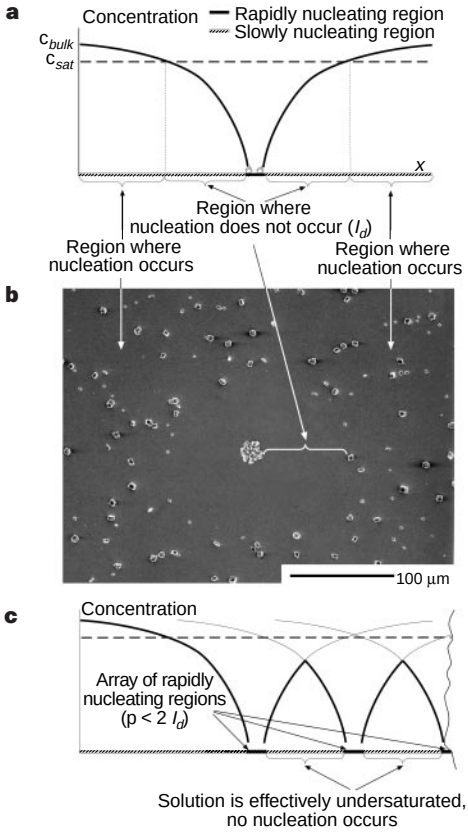

Figure 4 The effects of diffusion on nucleation. **a**, Calculated profiles of concentration of the crystallizing solution ($c(x)$) in the vicinity of the isolated, rapidly nucleating region, assuming mass transport to the preformed, growing crystal (crystals). The profiles were derived using the diffusion equation: $\partial c/\partial t = D\partial^2 c/\partial x^2$, and assuming zero concentration of solution at the surface of the crystallizing region (that is, assuming that all the ions that reach the surface of the crystal stick irreversibly). The dashed line corresponds to the concentration of the saturated solution, c_{sat}, below which nucleation on the slowly nucleating surface does not occur. In the region l_d where $c(x) < c_{sat}$, nucleation is, therefore, suppressed. Nucleation is allowed for distances from the rapidly nucleating region, $x > l_d$, where $c > c_{sat}$. For the nucleation on the methyl-terminated surfaces, c_{sat} is ~2.5 mM. **b**, SEM image of the pattern of calcite crystals grown on a methyl-terminated surface with one isolated carboxylate-terminated region, showing the depletion distance, $l_d \approx 80$ μm, in agreement with the value (~80–100 μm) calculated assuming $c_{bulk} = 25$ mM, c_{sat} = 2–2.5 mM and crystallization time $t = 30$ min. **c**, Calculated profiles of the concentration of the crystallizing solution in the vicinity of an array of rapidly nucleating regions with periodicity $p < 2l_d$. The effective concentration (bold lines) over the entire slowly nucleating region is then below c_{sat}. Crystallization will only take place on the rapidly nucleating regions, as shown in Fig. 1c.

© 1999 Macmillan Magazines Ltd

to control the microenvironment of the nucleation site and to manipulate near-surface gradients of concentrations of the crystallizing ions by patterning SAMs into rapidly and slowly nucleating regions.

The technique we report here gives us the ability to fabricate a large number of indistinguishable active nucleation regions, and to nucleate one crystal in each region. This should enable the study of fundamental aspects of the crystallization process by providing access to statistically significant numbers of nucleation events in highly controlled microenvironments. □

Received 20 October 1998; accepted 29 January 1999.

1. Heuer, A. H. *et al.* Innovative materials processing strategies: A biomimetic approach. *Science* **255,** 1098–1105 (1992).
2. Stupp, S. I. & Braun, P. V. Molecular manipulation of microstructures: Biomaterials, ceramics, and semiconductors. *Science* **277,** 1242–1246 (1997).
3. Zelinsky, B. J. J., Brinker, C. J., Clark, D. E. & Ulrich, D. R. *Better Ceramics Through Chemistry* (Materials Research Soc., Pittsburgh, 1990).
4. Mann, S. & Ozin, G. A. Synthesis of inorganic materials with complex form. *Nature* **382,** 313–318 (1996).
5. Landau, E. M., Levanon, M., Leiserowitz, L., Lahav, M. & Sagiv, J. Transfer of structural information from Langmuir monolayers to three-dimensional growing crystals. *Nature* **318,** 353–356 (1985).
6. Addadi, L., Moradian, J., Shay, E., Maroudas, N. G. & Weiner, S. A chemical model for the cooperation of sulfates and carboxylates in calcite crystal nucleation: relevance to biomineralization. *Proc. Natl Acad. Sci. USA* **84,** 2732–2736 (1987).
7. Belcher, A. M. *et al.* Control of crystal phase switching and orientation by soluble molusc-shell proteins. *Nature* **381,** 56–58 (1996).
8. Alper, M., Calvert, P. D., Frankel, R., Rieke, P. C. & Tirrell, D. A. *Materials Synthesis Based on Biological Processes* (Materials Research Soc., Pittsburgh, 1991).
9. Mann, S. *et al.* Crystallisation at inorganic-organic interfaces: Biominerals and biomimetic synthesis. *Science* **261,** 1286–1292 (1993).
10. Mann, S. Molecular tectonics in biomineralization and biomimetic materials chemistry. *Nature* **365,** 499–505 (1993).
11. Mann, S., Heywood, B. R., Rajam, S. & Birchall, J. D. Controlled crystallisation of $CaCO_3$ under stearic acid monolayers. *Nature* **334,** 692–695 (1988).
12. Heywood, B. R. & Mann, S. Template-directed nucleation and growth of inorganic materials. *Adv. Mat.* **6,** 9–20 (1994).
13. Bunker, B. C. *et al.* Ceramic thin-film formation on functionalized interfaces through biomimetic processing. *Science* **264,** 48–55 (1994).
14. Aizenberg, J., Black, A. J. & Whitesides, G. M. Controlling local disorder in self-assembled monolayers by patterning the topography of their metallic supports. *Nature* **394,** 868–871 (1998).
15. Gupta, V. K. & Abbott, N. L. Design of surfaces for patterned alignment of liquid crystals on planar and curved substrates. *Science* **276,** 1533–1535 (1997).
16. Berman, A. *et al.* Total alignment of calcite at acidic polydiacetylene films: Cooperativity at the organic-inorganic interface. *Science* **269,** 515–518 (1995).
17. Laibinis, P. E. *et al.* Comparison of the structures and wetting properties of self-assembled monolayers of *n*-alkanethiols on the coinage metal surfaces, Cu, Ag, Au. *J. Am. Chem. Soc.* **113,** 7152–7167 (1991).
18. Kumar, A., Abbott, N. A., Kim, E., Biebuyck, H. A. & Whitesides, G. M. Patterned self-assembled monolayers and meso-scale phenomena. *Acc. Chem. Res.* **28,** 219–226 (1995).
19. Xia, Y. & Whitesides, G. M. Soft Lithography. *Angew. Chem. Int. Edn. Engl.* **37,** 550–575 (1998).
20. Lippmann, F. *Sedimentary Carbonate Minerals* (Springer, Berlin, 1973).
21. Lowenstam, H. A. & Weiner, S. *On Biomineralization* (Oxford Univ. Press, 1989).
22. Barabási, A.-L. & Stanley, H. E. *Fractal Concepts in Surface Growth* (Cambridge Univ. Press, 1995).

Acknowledgements. This work has been supported in part by the ONR and DARPA. It used MRSEC Shared Facilities supported by the NSF.

Correspondence and requests for materials should be addressed to G.M.W. (e-mail: gwhitesides@gmwgroup.harvard.edu) and J.A. (e-mail: jaizenberg@lucent.com).

Complete asymmetric induction of supramolecular chirality in a hydrogen-bonded assembly

Leonard J. Prins, Jurriaan Huskens, Feike de Jong, Peter Timmerman & David N. Reinhoudt

Laboratory of Supramolecular Chemistry and Technology, MESA⁺ Research Institute, University of Twente, PO Box 217, 7500 AE Enschede, The Netherlands

Chirality at the supramolecular level involves the non-symmetric arrangement of molecular components in a non-covalent assembly[1,2]. Supramolecular chirality is abundant in biology, for example in the DNA double helix[3], the triple helix of collagen[4] and the α-helical coiled coil of myosin[5]. These structures are stabilized by inter-strand hydrogen bonds, and their handedness is determined by the configuration of chiral centres in the nucleotide or peptide backbone. Synthetic hydrogen-bonded assemblies have been reported that display supramolecular chirality in solution[6–8] or in the solid state[9–12]. Complete asymmetric induction of supramolecular chirality—the formation of assemblies of a single handedness—has been widely studied in polymeric superstructures[13,14]. It has so far been achieved in inorganic metal-coordinated systems[15–17], but not in organic hydrogen-bonded assemblies[18–20]. Here we describe the diastereoselective assembly of enantio-pure calix[4]arene dimelamines and 5,5-diethylbarbituric acid (DEB) into chiral hydrogen-bonded structures of one handedness. The system displays complete enantioselective self-resolution: the mixing of homomeric assemblies (composed of homochiral units) with opposite handedness does not lead to the formation of heteromeric assemblies. The non-covalent character of the chiral assemblies, the structural simplicity of the constituent building blocks and the ability to control the assembly process by means of peripheral chiral centres makes this system promising for the development of a wide range of homochiral supramolecular materials or enantioselective catalysts.

Previously we have shown by X-ray crystallography and ^{1}H NMR spectroscopy that assembly $\mathbf{1}_3$•DEB_6 exclusively forms as the staggered isomer **A** (D_3), which displays supramolecular chirality both in solution and in the solid state (see Fig. 1)[21,22]. In the absence of any other source of chirality, this isomer exists as a racemic mixture of the *M*- and *P*-enantiomers.

We have now found that assembly of 3 equivalents of the chiral calix[4]arene dimelamines (*R*,*R*)-**2** or (*S*,*S*)-**3**, having (*R*)- or (*S*)-1-phenylethylamine moieties, respectively, with 6 equivalents of DEB gives quantitatively the assemblies $\mathbf{2}_3$•DEB_6 (*M*-enantiomer) or $\mathbf{3}_3$•DEB_6 (*P*-enantiomer) (compounds **1**–**7** are shown in Fig. 1). The induction of helicity in both assemblies is complete (d.e. > 98%, where d.e. is diastereomeric excess) as judged from the single set of signals in the ^{1}H NMR spectra (CD_2Cl_2) (Fig. 2). None of the other possible diastereoisomeric assemblies (that is, (*P*)-$\mathbf{2}_3$•DEB_6 and (*M*)-$\mathbf{3}_3$•DEB_6) is present. Two-dimensional rotating frame Overhauser effect spectroscopy (ROESY) experiments correlate the absolute configuration of the substituents with the helicity: an (*R*)-substituent induces *M*-helicity, and an (*S*)-substituent induces *P*-helicity, in the assembly (Fig. 2d). We note that both assemblies are strongly active in circular dichroism (CD; $\Delta\epsilon_{max} \approx 100\,cm^2\,mmol^{-1}$, where $\Delta\epsilon_{max} = (\epsilon_L - \epsilon_R)_{286\,nm}$, Fig. 3a), while none of the individual components (*R*,*R*)-**2** or (*S*,*S*)-**3** show any significant CD activity ($\Delta\epsilon_{max} < 8\,cm^2\,mmol^{-1}$). The observed CD is thus clearly a direct result of assembly formation and not an intrinsic property of the individual components.

Complete induction of chirality was also observed for the (*S*)-alanine- and (*R*)-naphthyldimelamine assemblies (*P*)-$\mathbf{4}_3$•DEB_6 and (*M*)-$\mathbf{5}_3$•DEB_6 (d.e. > 98% according to ^{1}H NMR spectroscopy; data not shown) and seems to be a general phenomenon for this type of assembly. Moreover, complete chiral induction is also observed with peripheral chiral centres in the cyanurate components. Combination of achiral dimelamine **6** with chiral cyanurates (*R*)- or (*S*)-MePhCYA or amino acid-derived cyanurates (*S*)-PheCYA, (*S*)-ValCYA, or (*S*)-LeuCYA (see Fig. 1 for nomenclature) leads in all cases to diastereoselective assembly of $\mathbf{6}_3$•CYA_6 with d.e. values >98% according to ^{1}H NMR spectroscopy (data not shown). The CD spectra of the assemblies $\mathbf{2}_3$•DEB_6–$\mathbf{5}_3$•DEB_6 and $\mathbf{6}_3$•CYA_6 all display bisignate curves with remarkably large amplitudes. The peripheral chromophores (benzyl, carbonyl, naphthyl) only affect the intensity of the Cotton effect (CE) at lower wavelengths, while the CD curves are virtually identical above 250 nm (Fig. 3). The observed Cotton effects seem to be largely the result of exciton coupling between chromophores present in the core of the assemblies. Comparison of the different CD spectra suggests that the sign of the CD curve is a good probe for the helicity of the assembly.

© 1999 Macmillan Magazines Ltd